INTERNATIONAL JOURNAL FOR NUMERICAL METHODS IN ENGINEERING
Int. J. Numer. Meth. Engng 2006; **65**:1355–1377
Published online 11 October 2005 in Wiley InterScience (www.interscience.wiley.com). DOI: 10.1002/nme.1490

Thermal stress evaluation in the steel continuous casting process

J. M. Risso, A. E. Huespe and A. Cardona*, †

Centro Internacional de Métodos Computacionales en Ingeniería del INTEC, Consejo Nacional de Investigaciones Científicas y Técnicas—Universidad Nacional del Litoral, Güemes 3450, 3000 Santa Fe, Argentina

SUMMARY

Two numerical models for the thermal stress and plastic strain analysis in the solid shell at the initial stage of a steel continuous casting process, are presented and their performances evaluated. First, a numerical procedure based on a natural extension of the semi-analytical study proposed by Weiner and Boley (*J. Mech. Phys. Solids* 1963; **11**:145–154) is introduced and validated by comparison with their semi-analytical 1-D solution. The basic hypotheses of this model, and particularly the extended plane strain condition with uniform axial strain, are afterwards tested in more complex and realistic situations by comparing results with those obtained by an alternative numerical scheme presented by Fachinotti (*Doctoral Thesis*, Universidad Nac. Litoral, Argentina, 2001) and Fachinotti and Cardona (*Internal Report*, CIMEC, sent to *IJNME*, 2002). Finally, results of a typical and representative 3D simulation, corresponding to a slab continuous casting process, are shown. Copyright © 2005 John Wiley & Sons, Ltd.

KEY WORDS: continuous casting process; thermal stresses; solidification

1. INTRODUCTION

Internal cracking of steel products obtained by the continuous casting process may occur quite frequently, producing severe economic losses. Its prevention entails one of the most important issues in the development of this process, and motivates a number of research works. Various

*Correspondence to: Alberto Cardona, CIMEC-INTEC, Güemes 3450, 3000 Santa Fe, Argentina.
†E-mail: acardona@intec.unl.edu.ar

Contract/grant sponsor: Agencia Nacional de Promoción Científica y Tecnológica; contract/grant number: PID 99-76
Contract/grant sponsor: Consejo Nacional de Investigaciones Científicas y Técnicas; contract/grant number: PIP 0266/99
Contract/grant sponsor: Universidad Nacional del Litoral; contract/grant number: CAI+D PE 214

Received 23 August 2004
Revised 5 April 2005
Accepted 20 June 2005

interacting factors, including thermal, mechanical and metallurgical ones, are recognized to be the cause of cracking.

Experimental works, such as Yamanaka *et al*. [1], Kim *et al*. [2], Won *et al*. [3, 4], noted the existence of a correlation between internal cracking and a critical amount of strain developed between the so-called zero strength and zero ductility temperatures. Bernard *et al*. [5] proposed a criterion based on peak stresses, instead of strain values, to determine cracking susceptibility. Clyne *et al*. [6] remarked the importance of alloy constitution and microsegregation of solute in determining the susceptibility of steel to solidification cracking. Nakagawa *et al*. [7] presented experimental results and proposed a numerical procedure to understand the influence of factors such as strain rate, progress of solidification and chemical composition among others. It is therefore observed that, regardless of criteria, cracking prediction models use the mechanical stress–strain state at temperatures close to solidification as a fundamental input.

In this paper we analyse the stress–strain state of the solid shell formed in the early stage of steel continuous casting processes, in which some types of cracks are believed to be produced, by using specially developed finite element numerical methods.

Several methods for analysing this problem have been presented in the literature. Weiner and Boley [8] developed a simplified semi-analytical procedure to give a rough approximation of the evolution of stresses in this zone. Kristiansson [9] presented a finite element model in which a strip of elements were used to model a slice of the casting. Boundary conditions were imposed restricting axial displacements to be equal above (and below) the slice. *This hypothesis is similar to that adopted by Weiner and Boley in their semianalytical study*. Two-dimensional approaches based on a plane strain hypothesis perpendicular to the casting direction have been used in the literature for thermal stress evaluation of continuous casting simulations [4, 10–13]. Nevertheless, these slice models are questionable to reproduce accurately the 3D mechanical state at some critical zones, like the mould exit in slab continuous casting, where stress state is clearly fully 3D. One of the main objectives of this work is to determine the magnitude of these differences.

In Section 2.1 we develop an improved 2D formulation to solve the thermal-mechanical problem using a hypothesis of plane strain normal to the direction of casting with uniform (and nonzero) axial strain ε_z. This hypothesis is fully consistent with the original proposal of Weiner and Boley and has also been followed by Thomas and coworkers [14–19], who called it *Generalized Plane Strain* hypothesis. We propose instead the name two-dimensional *extended plane strain condition* (EPSC) to avoid confusions with a kinematic hypothesis used in plate analysis (see References [20, 21]) which has been given that name. In Section 3 we compare the results obtained for the one-dimensional EPSC case, with those reported in the above-mentioned studies.

In Section 2.2, we present an alternative Eulerian–Lagrangian procedure where no EPSC condition is assumed (see References [22, 23]). Section 4 presents a comparative analysis of results obtained with both models for the simulation of a billet continuous casting process. This allows us to get an estimation of the error introduced by the EPSC assumption, particularly in the region close to the mould exit. In both cases, the problem of thermal conduction with phase change was solved following the procedure we previously proposed [24, 25].

In Section 5 we present detailed results of simulation of a slab continuous casting, obtained by using the EPSC model. This final example illustrates the power of the developed EPSC method to deal with large continuous casting simulations. We make also some estimations of CPU time gains in Section 6.

2. DESCRIPTION OF THE MECHANICAL PROBLEM

Thermal stresses in the solid shell result from a complex coupling of fluid flow, heat flow, phase-change and solid deformation phenomena [26, 27]. Let us assume in a first approach a stationarity condition for the thermal analysis with a strand average casting velocity $\mathbf{v}_c$ uncoupled from the mechanical variables. Those aspects introducing the mechanical coupling into the energy equation are not addressed in this work, since they are not relevant for the discussion (interested readers may look at Reference [28] where we presented a coupled thermal-mechanical formulation of continuous casting problems). After determining the temperature field, we make a stress analysis considering a nonlinear material behaviour with parameters strongly dependent on temperature.

It is recognized that finite element techniques, with standard constitutive material modelling, yield good solutions in thermal stress analysis even when the solid is subjected to temperatures near the solidification ones. However, there are particular aspects in the formulation of continuous casting problems that need to be carefully considered.

Let us assume a Lagrangian description for the mechanical simulation of this process (Figure 1). We can consider three different configurations for every material point and its neighbourhood:

(i) the reference configuration (B), in which the particle label is assigned;
(ii) the (intermediate) natural configuration (B^0) which corresponds to that state where the material point solidified just below the zero strength temperature (ZST), and started to develop mechanical strength;
(iii) the current configuration (B^t).

Note that, since the solidification time instant is not the same one for all points in the domain of analysis, each material point has its own (intermediate) natural configuration. The ZST is defined as the minimum temperature amongst those at which strength is zero [7]. Temperatures

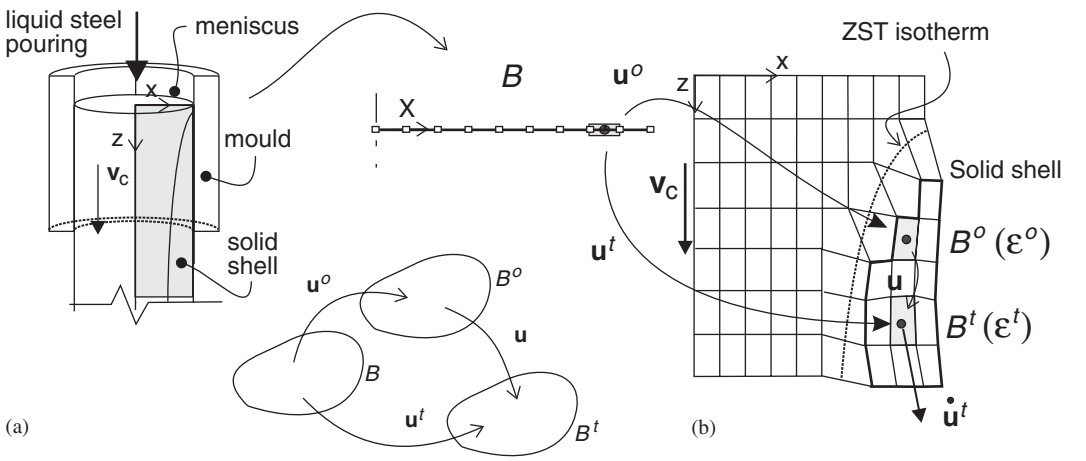

Figure 1. Reference (B), natural (B^0) and current (B^t) body configurations in the continuous casting problem.

corresponding to solid fraction values ranging from 0.65 to 0.80 are commonly used for this parameter in the literature [1, 3, 15].

By denoting as $\mathbf{u}^o$ the displacement from the reference to the natural configuration, $\mathbf{u}^t$ the displacement from the reference to the current configuration and $\mathbf{u}$ the displacement from the natural to the current configuration, we can write:

$$\mathbf{u}^t = \mathbf{u} + \mathbf{u}^o \tag{1}$$

Usually, when a finite element procedure is used, the mesh is defined in the reference configuration as depicted schematically in Figure 1(b). In this picture we represent the reference domain B as the set of points at the top of the mould at time $t = 0$. The object of the analysis is the determination of strains and stresses in this set of points as time proceeds.

Let us consider that $\mathbf{X}$ and $\mathbf{x}^o$ are coordinate systems in the reference and natural configurations, respectively. As a consequence of the assumption of small deformations we introduced to describe motion, and by assuming the existence of the intermediate deformation gradient in the neighbourhood of every point, we have:

$$\nabla_{\mathbf{X}} \mathbf{x}^o \approx \mathbf{1}$$

The same assumption allows us to evaluate the strain $\boldsymbol{\varepsilon} = \nabla^{\text{sym}}_{\mathbf{x}^o} \mathbf{u}$, related to the motion from the natural to the final configurations, by the following approximation:

$$\boldsymbol{\varepsilon} = \nabla^{\text{sym}}_{\mathbf{x}^o} \mathbf{u} \approx \nabla^{\text{sym}}_{\mathbf{X}} \mathbf{u} \tag{2}$$

By taking gradients in Equation (1) and using the assumptions stated above, we can verify the validity of the additive decomposition of strains:

$$\boldsymbol{\varepsilon}^t = \boldsymbol{\varepsilon} + \boldsymbol{\varepsilon}^o \tag{3}$$

where $\boldsymbol{\varepsilon}^t = \nabla^{\text{sym}}_{\mathbf{X}} \mathbf{u}^t$ is the strain tensor at the actual configuration (time t) with respect to the reference configuration, and $\boldsymbol{\varepsilon}^o = \nabla^{\text{sym}}_{\mathbf{X}} \mathbf{u}^o$ is the strain at the natural configuration with respect to the reference one.

The mechanical strain $\boldsymbol{\varepsilon}_{\text{M}}$ is computed subtracting the thermal strain $\boldsymbol{\varepsilon}_\theta$ from the actual strain $\boldsymbol{\varepsilon}$:

$$\boldsymbol{\varepsilon}_{\text{M}} = \boldsymbol{\varepsilon} - \boldsymbol{\varepsilon}_\theta, \quad \boldsymbol{\varepsilon}_\theta = \beta_{(\theta)} \mathbf{1} \tag{4}$$

with $\beta_{(\theta)}$ being the thermal expansion function. Stresses in the solid shell are directly related to the mechanical strains, through the constitutive material law.

Since an objective of this work was the comparison between 2D EPSC and 3D formulations, the solid shell material constitutive response was represented simply by using a standard elastoplastic model. The use of more sophisticated laws, like viscoplastic ones [29, 30], would not have changed the conclusions of this work (a full comparison between elastoplastic and viscoplastic models for the continuous casting problem has been reported in References [22, 31]).

By adopting the classical J_2 theory with isotropic hardening, the stress–strain relation results [32]:

$$\boldsymbol{\sigma} = \mathbf{C}^{\text{e}}_{(\theta)} \cdot (\boldsymbol{\varepsilon}_{\text{M}} - \boldsymbol{\varepsilon}^{\text{p}}_{\text{M}}) \tag{5}$$

where $\boldsymbol{\varepsilon}_{\mathrm{M}}^{\mathrm{p}}$ is the plastic mechanical strain and $\mathbf{C}_{(\theta)}^{\mathrm{e}}$ is the elastic constitutive tensor

$$\mathbf{C}^{\mathrm{e}} = \frac{E_{(\theta)}}{(1+\nu_{(\theta)})}\mathbf{I} + \frac{\nu_{(\theta)}E_{(\theta)}}{(1+\nu_{(\theta)})(1-2\nu_{(\theta)})}(\mathbf{1}\otimes\mathbf{1})$$

with $(E_{(\theta)}, \nu_{(\theta)})$ the (temperature dependent) Young modulus and Poisson coefficient and $\mathbf{1}$, $\mathbf{I}$ the second and fourth order identity tensors. Isotropic strain hardening is described using a scalar internal stress-like variable q, which is related to its conjugate internal variable κ through the plastic modulus H:

$$\dot{q} = -H_{(\theta)}\dot{\kappa} \tag{6}$$

Classical associative flow laws define the evolution of the strain-like internal variables:

$$\dot{\boldsymbol{\varepsilon}}_{\mathrm{M}}^{\mathrm{p}} = \lambda\mathbf{n}, \quad \dot{\kappa} = \lambda\sqrt{\tfrac{2}{3}} \tag{7}$$

where λ is the plastic multiplier and $\mathbf{n}$ the direction of the plastic strain rate, defined by the deviatoric stress $\boldsymbol{\sigma}_{\mathrm{dev}}$:

$$\mathbf{n} = \frac{\boldsymbol{\sigma}_{\mathrm{dev}}}{\|\boldsymbol{\sigma}_{\mathrm{dev}}\|} \tag{8}$$

Finally, we have the consistency relations:

$$\lambda \geqslant 0, \quad \phi(\boldsymbol{\sigma}, q, \theta) \leqslant 0, \quad \phi\lambda = 0 \tag{9}$$

with the yield criteria $\phi(\boldsymbol{\sigma}, q, \theta)$, which in our case is von Mises yield surface:

$$\phi(\boldsymbol{\sigma}, q, \theta) = \sqrt{\boldsymbol{\sigma}_{\mathrm{dev}} \cdot \boldsymbol{\sigma}_{\mathrm{dev}}} - \sqrt{\tfrac{2}{3}}(\sigma_{y(\theta)} - q) \tag{10}$$

In this equation, $\sigma_{y(\theta)}$ is the yield stress. We remark that for a correct representation of the steel constitutive behaviour in the zone of interest, it is mandatory to account for the strong dependence of the material parameters on temperature. The above equations make this characteristic evident.

2.1. EPSC with uniform axial strain: pure Lagrangian description

The instantaneous velocity of a point in the solid shell $\dot{\mathbf{u}}^t$ can be seen as the result of the addition of two terms: the average casting velocity $\mathbf{v}_{\mathrm{c}}$ in the direction of axis z, and a relative velocity $\dot{\mathbf{u}}^r$ defined with respect to an observer moving with the velocity $\mathbf{v}_{\mathrm{c}}$ (see Figure 1):

$$\dot{\mathbf{u}}^t = \mathbf{v}_{\mathrm{c}} + \dot{\mathbf{u}}^r, \quad \dot{\mathbf{u}}^r = (\dot{u}_x^r, \dot{u}_y^r, \dot{u}_z^r) \tag{11}$$

The EPSC assumes that $\dot{\varepsilon}_z = \partial\dot{u}_z^r/\partial z$ does not depend on the coordinates (x, y), where z coincides with the direction of casting (see Figure 2). Furthermore, it is assumed that $\dot{\varepsilon}_{xz} \approx \dot{\varepsilon}_{yz} \approx 0$. Both restrictions impose that $\dot{u}_x^r$ and $\dot{u}_y^r$ must be independent of the coordinate z. Note, however, that these assumptions are clearly not valid in some regions of the solid shell.

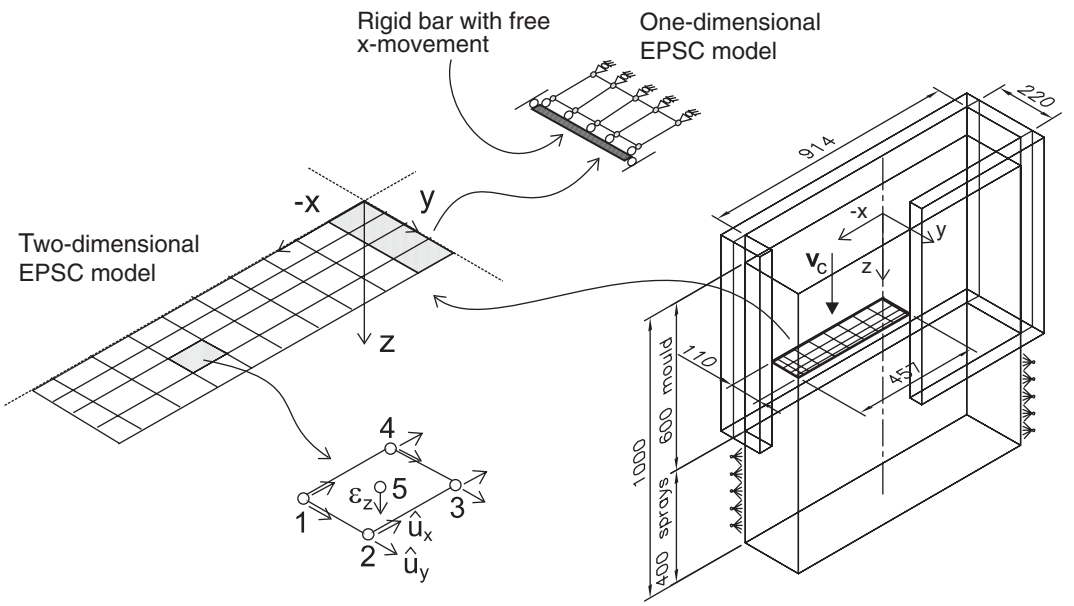

Figure 2. EPSC: model of a slab continuous casting process.

The term $\dot{\varepsilon}_z$ can be implicitly treated in the analysis by considering the equilibrium equation in the z direction. The upper section of the casting machine (pouring section) is modelled as a traction free boundary. Frictional forces between solid shell and mould may be neglected, since for normal casting speeds and continuous casting flux powders, shear stresses are smaller than 0.02 MPa [33, 34]. Also, normal stresses σ_z generated by the weight of liquid and solid shell are typically smaller than 0.02 MPa and may be neglected as well. Then, resultant forces in every transversal section are:

$$\int_A \sigma_z(x, y)\, \mathrm{d}x\, \mathrm{d}y \approx 0 \tag{12}$$

Using this assumption, we may project the 3-D model to a plane problem and afterwards treat it numerically as if it were a pure 2-D mechanical state.

Note that the equations to be solved in this model result from the transformation of the stationary advection hyperbolic problem to a parabolic one.

2.1.1. The two-dimensional EPSC finite element. We implement the two-dimensional EPSC with uniform axial strain and with zero resultant transversal forces, by adopting a reference domain lying on the plane (x, y) (Figure 2). The domain is discretized using standard bilinear quadrilateral four-nodes finite elements, which include an additional degree-of-freedom (d.o.f.) that accounts for the axial component of strain ε_z. We call this element the *QUAD4_EPSC*

element. Its strain–displacement matrix $\mathbf{B}$ is written as

$$\mathbf{B}^{4\times 9}=\begin{pmatrix} \mathbf{B}_1^{\mathrm{qst}} & \mathbf{B}_2^{\mathrm{qst}} & \mathbf{B}_3^{\mathrm{qst}} & \mathbf{B}_4^{\mathrm{qst}} & \mathbf{0} \\ \mathbf{0} & \mathbf{0} & \mathbf{0} & \mathbf{0} & 1 \end{pmatrix} \tag{13}$$

where $\mathbf{B}_i^{\mathrm{qst}}$ is the ith block of the standard strain–displacement matrix of the bilinear quadrilateral element:

$$\mathbf{B}_i^{\mathrm{qst}}=\begin{pmatrix} \dfrac{\partial N_i}{\partial x} & 0 \\ 0 & \dfrac{\partial N_i}{\partial y} \\ \dfrac{\partial N_i}{\partial y} & \dfrac{\partial N_i}{\partial x} \end{pmatrix}$$

and $N_i(x, y)$ is the corresponding shape function of node i. The generalized displacements elemental vector results:

$$\hat{\mathbf{q}}^{\mathrm{T}}=[u_x^1 \;\; u_y^1 \;\; \ldots \;\; u_x^4 \;\; u_y^4 \;\; \hat{\varepsilon}_z] \tag{14}$$

The additional d.o.f. $\hat{\varepsilon}_z$ is shared by all elements in the mesh. It is numbered as the last global d.o.f. in the system. In this way, the coupling introduced by the equilibrium equation (12) does not substantially change the skyline of the structural stiffness matrix and therefore, the computational cost remains equivalent to that of a 2-D analysis.

The strain $\boldsymbol{\varepsilon}^o$ is computed the first time that all nodal temperatures of the considered element fall below the ZST, and is stored at the finite element Gauss point as an additional tensorial internal variable.

In this model, the solid shell domain changes with time. This fact introduces some difficulties concerning the mesh definition for the FE analysis. The procedure we have implemented consists in defining a mesh that describes the complete domain, including the liquid and mushy zones. Nodes with temperature above the ZST are initially fixed. In subsequent time steps, when the nodal temperatures fall below the ZST, nodal d.o.f.s are freed and the stiffness contribution of the solidified zone is taken into consideration (see Figure 3). This strategy was implemented into the object-oriented finite element code Oofelie [35, 36]), taking advantage of its ability for managing d.o.f.s.

Remarks

- The described numerical model does not predict the real displacement field inside the solid shell, because the displacement field of the natural configuration is not known. However, displacements in the natural configuration of the elements located on the shell surface are known and equal to zero, so the real displacements of the shell surface are correctly approximated. This is an important fact since this allows to verify the mould taper and also to impose contact restrictions between the external face of the solid shell and the mould.
- The technique of substraction of the strain term $\boldsymbol{\varepsilon}^o$ from the total strain $\boldsymbol{\varepsilon}^t$ must be emphasized for its simplicity and accuracy. Stress computations based on total strain,

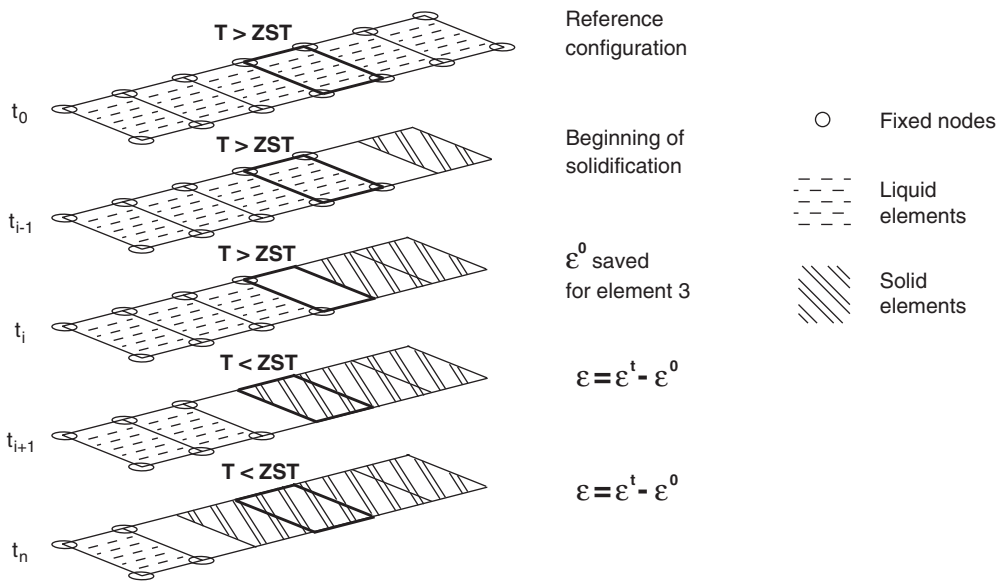

Figure 3. EPSC model: managing the d.o.f.s and strains in the finite element mesh as time proceeds.

without substraction of the initial strain $\boldsymbol{\varepsilon}^o$, give completely unrealistic results, a fact that may be verified by comparison with results obtained by using the semi-analytical formulation of Weiner and Boley. We note also that this approach is less expensive than that used by other authors based on recording flow strain for liquid elements [37].

2.2. Mechanical model based on an Eulerian–Lagrangian description

In this section we describe an alternative model for analysing the mechanical stress state in continuous casting problems. We have used it for the numerical simulation of continuous casting billets, where symmetry of revolution in the thermal and mechanical problems is assumed. Its generalization to 3D problems is straightforward.

This model removes the hypothesis of $\dot{\varepsilon}_z$ uniformity in z-constant planes, typical of the EPSC. The reference configuration is a 2-D domain as shown in Figure 4, which only represents the solid shell. The x coordinate represents the billet radial direction.

The analysis is performed at time t assuming, as previously done, stationary state. The material rate of all variables (e.g. the plastic mechanical strain rate), can be determined by the advection term:

$$\dot{\boldsymbol{\varepsilon}}_{\mathrm{M}}^{\mathrm{p}} = \mathbf{v}_{\mathrm{c}} \cdot \nabla \boldsymbol{\varepsilon}_{\mathrm{M}}^{\mathrm{p}} \tag{15}$$

Let Γ be a streamline of the flow defined by the mean casting velocity $\mathbf{v}_{\mathrm{c}}$, and let $(\mathbf{x}_1, \mathbf{x}_0)$ be two points lying along this curve which are related by: $\mathbf{x}_1 = \mathbf{v}_{\mathrm{c}} \Delta t + \mathbf{x}_0$. Let also P be a material point staying at position $\mathbf{x}_1$ at time t. Note that the mechanical plastic strain at this point at time $t - \Delta t$ is equal to the mechanical plastic strain at a point located at $\mathbf{x}_0$ at the

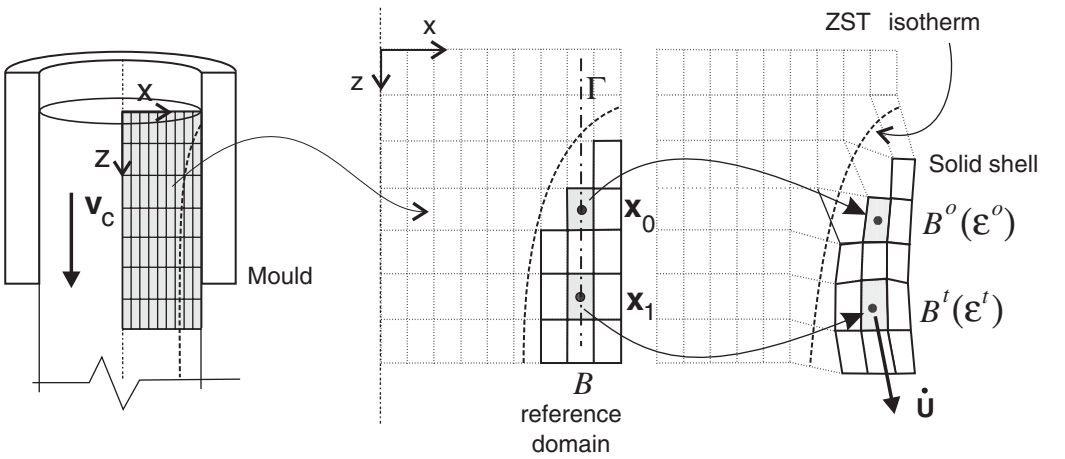

Figure 4. Eulerian–Lagrangian model for simulating the continuous casting of round billets.

current time t:

$$\boldsymbol{\varepsilon}^{\mathrm{p}}_{\mathrm{M}(P,t-\Delta t)} = \boldsymbol{\varepsilon}^{\mathrm{p}}_{\mathrm{M}(\mathbf{x}_0,t)} \tag{16}$$

Then, the mechanical plastic strain rate $\dot{\boldsymbol{\varepsilon}}^{\mathrm{p}}_{\mathrm{M}}$ (Equation (15)) can be approximated incrementally by:

$$\dot{\boldsymbol{\varepsilon}}^{\mathrm{p}}_{\mathrm{M}} \approx \frac{\boldsymbol{\varepsilon}^{\mathrm{p}}_{\mathrm{M}(P,t)} - \boldsymbol{\varepsilon}^{\mathrm{p}}_{\mathrm{M}(P,t-\Delta t)}}{\Delta t} \approx \|\mathbf{v}_{\mathrm{c}}\| \frac{\boldsymbol{\varepsilon}^{\mathrm{p}}_{\mathrm{M}(\mathbf{x}_1,t)} - \boldsymbol{\varepsilon}^{\mathrm{p}}_{\mathrm{M}(\mathbf{x}_0,t)}}{\|\mathbf{x}_1 - \mathbf{x}_0\|} \tag{17}$$

which allows us to rewrite the elastoplastic material model equations (5)–(10) in incremental form as follows:

$$\boldsymbol{\sigma}_{(\mathbf{x}_1)} = \mathbf{C}^{\mathrm{e}}_{(\theta)} \cdot (\boldsymbol{\varepsilon}_{\mathrm{M}(\mathbf{x}_1)} - \boldsymbol{\varepsilon}^{\mathrm{p}}_{\mathrm{M}(\mathbf{x}_1)}) \tag{18}$$

$$\boldsymbol{\varepsilon}^{\mathrm{p}}_{\mathrm{M}(\mathbf{x}_1)} = \boldsymbol{\varepsilon}^{\mathrm{p}}_{\mathrm{M}(\mathbf{x}_0)} + \Delta\boldsymbol{\varepsilon}^{\mathrm{p}}_{\mathrm{M}(\mathbf{x}_1)} \tag{19}$$

$$\Delta\boldsymbol{\varepsilon}^{\mathrm{p}}_{\mathrm{M}} = \Delta\lambda\mathbf{n}, \quad \mathbf{n} = \frac{\boldsymbol{\sigma}_{\mathrm{dev}(\mathbf{x}_1)}}{\|\boldsymbol{\sigma}_{\mathrm{dev}(\mathbf{x}_1)}\|} \tag{20}$$

$$q_{(\mathbf{x}_1)} = q_{(\mathbf{x}_0)} + \Delta q_{(\mathbf{x}_1)}, \quad \Delta q_{(\mathbf{x}_1)} = -H_{(\theta)}\Delta\kappa_{(\mathbf{x}_1)} \tag{21}$$

$$\Delta\kappa_{(\mathbf{x}_1)} = \Delta\lambda\sqrt{\tfrac{2}{3}} \tag{22}$$

$$\Delta\lambda \geqslant 0, \quad \phi_{(\boldsymbol{\sigma}(\mathbf{x}_1),q(\mathbf{x}_1),\theta)} \leqslant 0, \quad \phi\Delta\lambda = 0 \tag{23}$$

The mechanical strain $\boldsymbol{\varepsilon}_{\mathrm{M}}$ is determined by using Equation (4), where $\boldsymbol{\varepsilon}$ can be computed from the total displacement field (see Equation (2)).

The arbitrary choice of point $\mathbf{x}_0$ determines the incremental variable $\Delta\lambda$. If a viscous material model were considered, the incremental time Δt would be explicitly included in the above equation, but the basic assumptions would still remain valid.

2.2.1. Implementation of the Eulerian–Lagrangian axisymmetric 2-D model. From the numerical point of view, this model is easily implemented in a standard elasto-plastic finite element code when structured meshes are used. For this purpose it is just necessary to include a pointer to the preceding element along the same streamline Γ for every element in the mesh. In this way, a one-to-one relation is defined between every Gauss point of the mesh with another Gauss point belonging to the preceding element. The constitutive equations ((18)–(23)) use this relation to obtain the historical variables at the previous time, as pointed out by Equation (17).

The finite element mesh only describes the solid shell domain, i.e. the points with temperature below the ZST, which in the mechanical analysis are known beforehand from the thermal analysis.

The discrete equilibrium equations are solved by using a standard Newton method. The Jacobian matrix corresponds to that obtained from an equivalent purely Lagrangian elastoplastic quasi-static incremental problem (see for instance Reference [32]).

3. VALIDATION OF THE NUMERICAL MODEL

Let us consider the early stage of a slab continuous casting process (Figure 2), and particularly the region corresponding to the central part of the wide face in the solid shell. Thermal stresses arising there can be evaluated by imposing the EPSC to the z and x directions, because there exists a traction free condition on all vertical slab sides. Of course, this hypothesis neglects any effect of shell curvature on strains.

Following this particular assumption, Weiner and Boley [8] calculated a simplified one-dimensional semi-analytical solution. The thermal problem they solved corresponds to the Neumann's classical one, a phase change 1D problem with uniform initial temperature θ_1 (the liquidus temperature) and fixed temperature $\theta_o < \theta_1$ on one end (which corresponds to the shell surface in Figure 2). They took an elastic-perfectly plastic material model for the mechanical problem, with a constant Young modulus E and yield stress σ_y varying linearly with temperature:

$$\sigma_{y(\theta)} = \sigma_y^o \frac{\theta_1 - \theta}{\theta^o}, \quad \theta \leqslant \theta_1 \tag{24}$$

where σ_y^o is the yield stress at temperature θ_o and $\theta^o = \theta_1 - \theta_o$.

The Neumann's solution introduces a characteristic length $\bar{y} = p\sqrt{t}$, where t denotes time and the parameter p is given by

$$p = 2\sqrt{K_s}\gamma, \quad K_s = \frac{\kappa}{\rho C_p}, \quad \gamma \approx \sqrt{\frac{\theta^o C_p}{2L}} \quad (\gamma^2 \ll 1) \tag{25}$$

The thermal diffusivity K_s is the ratio of conductivity κ to density ρ and specific heat C_p, while L is the latent heat.

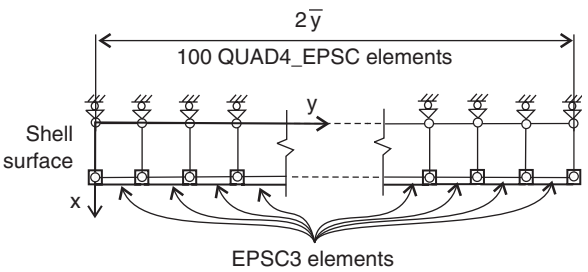

Figure 5. Finite element model for the 1-D numerical validation test (see Figure 2).

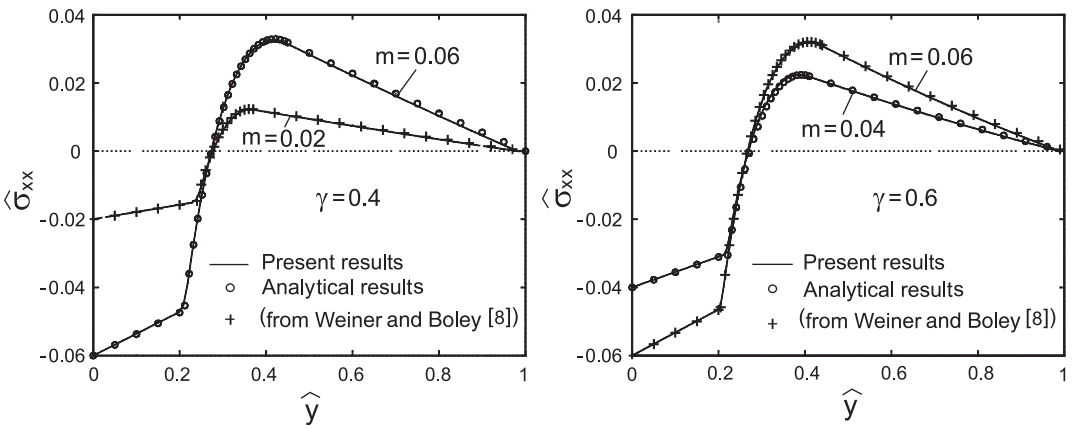

Figure 6. Stress distribution along the $\hat{y}$ coordinate, 1-D problem [8]. Comparison of semianalytical and numerical solutions.

Weiner and Boley introduced also the dimensionless quantities:

$$\hat{y} = \frac{y}{\bar{y}}, \quad \hat{\theta} = \frac{\theta - \theta_1}{\theta^o}$$

$$\hat{\sigma} = \frac{(1-v)\sigma}{\alpha E \theta^o}, \quad \hat{\sigma}_y = \frac{(1-v)\sigma_y}{\alpha E \theta^o} = -m\hat{\theta}, \quad m = \frac{(1-v)\sigma_y^o}{\alpha E \theta^o}$$

where α is the thermal expansion coefficient and v the Poisson's ratio.

We have solved this problem with the finite element procedure described in Subsection 2.1.1 by assuming one-dimensional EPSC conditions along directions z and x. The FE mesh consists of 100 QUAD4_EPSC elements, as shown in Figure 5. The EPSC condition in the x direction ($\varepsilon_x = \text{constant}$) is imposed via Lagrange multipliers (elements called EPSC3 in the figure) placed on the bottom side and constraining all nodal x-displacements to be identical.

Figure 6 compares the semi-analytical results with the numerical ones. The curves plot the nondimensional stress component $\hat{\sigma}_{xx} (= \hat{\sigma}_{zz})$ along the nondimensional $\hat{y}$-line (surface shell

depth) for different values of parameters m and γ. The agreement of the numerical FE solution with the semi-analytical one is evident from the figure.

It should be noted that this semi-analytical solution gives a maximum tensile (compressive) stress which is constant in time. Therefore, these values do not change with the axial coordinate. This behaviour is due to the particular thermal boundary conditions adopted (which correspond to a similarity solution) in the mentioned semi-analytical study. However, as Weiner and Boley pointed out, the stress distribution trend is similar to that observed in more complex solidification problems.

4. ANALYSIS OF CONTINUOUS CASTING OF ROUND BILLETS

In this section, we analyse the early stage in the process of continuous casting of a round billet, including the mould exit zone. We compare FE results obtained using an EPSC model with those we got using the Eulerian–Lagrangian axisymmetric one of Section 2.2. Tests were made using a 0.3% C carbon steel.

Figure 7(a) gives a schematic diagram of the problem geometry while Figure 7(b) displays the material parameters as a function of temperature. In the present simulation we have not included the effect due to the solid–solid phase transformation volumetric change. However, it can be taken into account implicitly in the curve $\beta(\theta)$ [28, 38]. The material parameters for the thermal problem are specified in Table I (taken from Reference [39]).

The liquid conductivity κ_l is larger than the solid conductivity κ_s to take into account turbulence in the liquid pool, as proposed in Reference [38]. The casting speed v_c was assumed to be 1.6 m/s, and the boundary thermal conditions were:

(a) prescribed flux in the mould–slab interface (using Savage–Pritchard law [40, 41]):

$$q(\mathrm{MW/m^2}) = -\left(3.071 - 0.361\sqrt{\frac{\Delta z}{v_c}}\right) \tag{26}$$

where Δz(m) is the z-distance from the meniscus;

Table I. Material and problem data for the round billet continuous casting process.

Parameter	Symbol	Value
Density	ρ	7200 kg/m^3
Specific heat	C_p	680 J/(kg °C)
Latent heat	L	272 000 J/kg
Conductivity (solid)	κ_s	34 W/(m °C)
Conductivity (liquid)	κ_l	68 W/(m °C)
Solidus temp.	θ_s	1490°C
Liquidus temp.	θ_l	1501°C
Zero strength temp.	ZST	1495°C
Pouring temp.	θ_p	1530°C

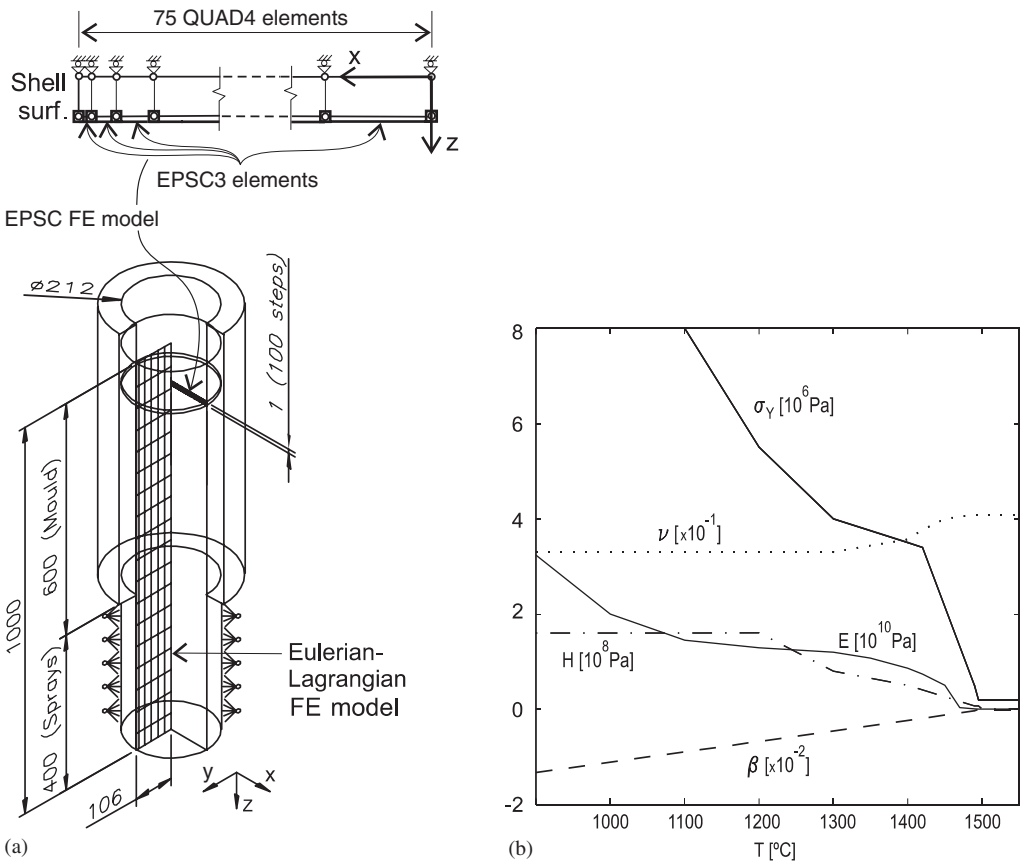

Figure 7. Round billet continuous casting simulation: (a) geometry and EPSC model (lengths are expressed in mm); and (b) temperature-dependent material parameters; E: Young's modulus, v: Poisson's ratio, H: Hardening modulus, σ_Y: yield stress and β: thermal expansion function.

(b) convective flux, due to sprays below the mould exit [42] (using a convection coefficient $h_s = 0.5\,\mathrm{MW/(m^2\,°C)}$ and $\theta_{\mathrm{spray}} = 40°\mathrm{C}$):

$$q = h_s(\theta_{\mathrm{surface}} - \theta_{\mathrm{spray}}) \tag{27}$$

A J_2 plasticity material model with isotropic hardening [31] is again used for the mechanical analysis of the solid shell.

Meshes for both models were designed in such a way that they have similar time–space discretizations:

- The EPSC model was solved by using a finite element mesh of 75 *standard* QUAD4 axisymmetric elements, as shown in Figure 7. The mesh was refined close to the billet surface. The extended plane strain condition was imposed using Lagrange multipliers (elements EPSC3 in the figure).

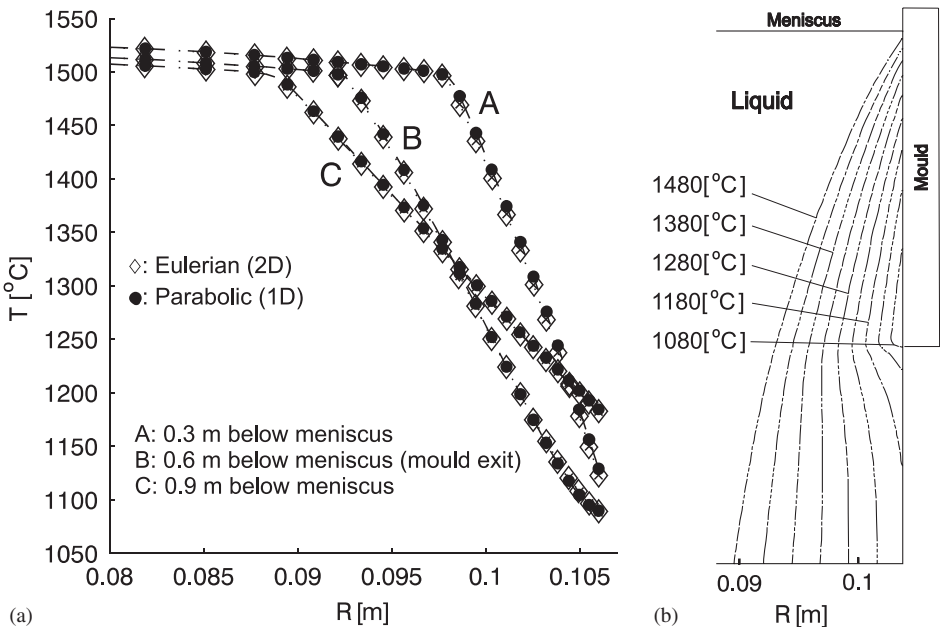

Figure 8. Round billet continuous casting simulation: (a) evolution of temperatures across radial axis R; and (b) temperature profiles in the solid shell.

- The Eulerian–Lagrangian model used a 2D mesh with the same radial distribution of elements as in the EPSC model mesh. The axial direction was discretized with 100 elements. The incremental time step in the EPSC model was defined to match the axial discretization of the Eulerian–Lagrangian scheme.

Figure 8(a) shows the temperature distribution across the billet radius in different positions, obtained with two different thermal models:

- The first model is a parabolized one-dimensional procedure, in which heat conduction in the z direction is neglected.
- The second model is a fixed domain method, that corresponds to an Eulerian (hyperbolic) two-dimensional description [25].

We remark the natural identification of these two methods with the mechanical EPSC and Eulerian–Lagrangian models, respectively. Both results are in a very good agreement, predicting a severe reheating in the surface shell at the mould exit zone.

When comparing the axial (or circumferential) stresses (Figure 9(a)), we find again a good agreement between both results, except in those sections placed near the mould exit. There, a slightly incorrect stress prediction of the EPSC model is produced because of the abrupt change of the thermal boundary conditions.

The same behaviour is found for the radial stresses (even considering that radial stresses are one order of magnitude lower than axial or circumferential stresses). Figure 9(b) shows a noticeable difference in the predicted tensile peak stress in the zone close to the mould exit. However, this peak stress is developed in a very thin superficial region.

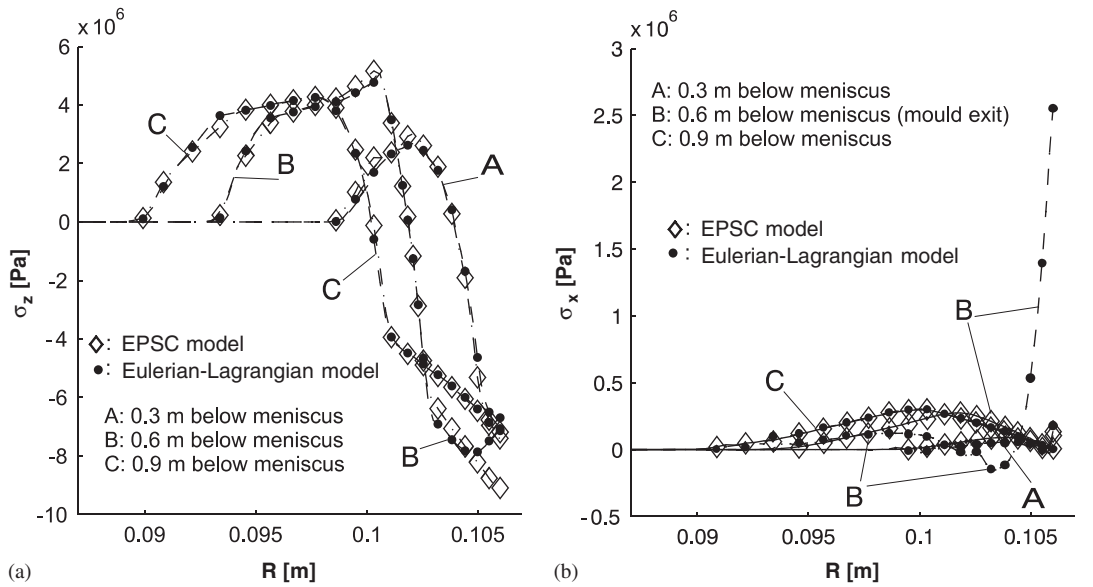

Figure 9. Round billet continuous casting simulation. Comparison of computed: (a) axial; and (b) radial stresses.

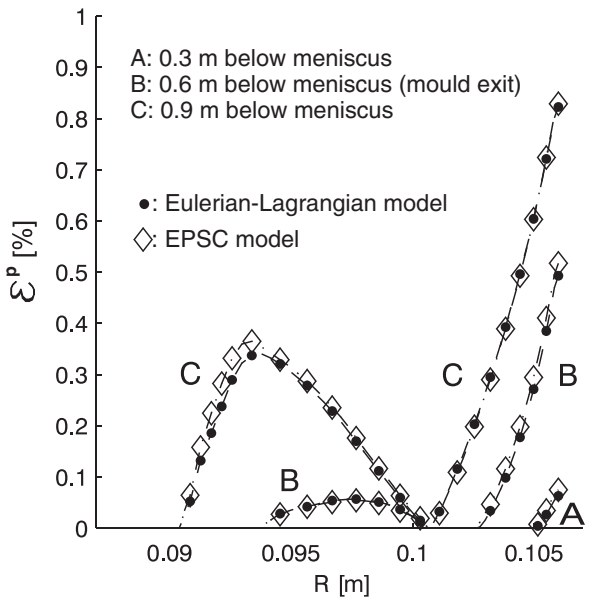

Figure 10. Round billet continuous casting simulation. Comparison of computed equivalent plastic strains.

Figure 10 shows good agreement between solutions for the predictions of equivalent plastic strains. This observation has important consequences when the crack criterion is based on the total applied strain (see Reference [1]).

5. ANALYSIS OF CONTINUOUS CASTING OF SLABS

A thermomechanical analysis of a slab continuous casting process is presented. Figure 11 displays the schematic diagram and geometrical data of the simulated problem. The cast material is a low carbon steel [43]. Figure 11 gives a schematic diagram of the problem geometry. Table II specifies the main material parameters for the modelling of the thermal problem.

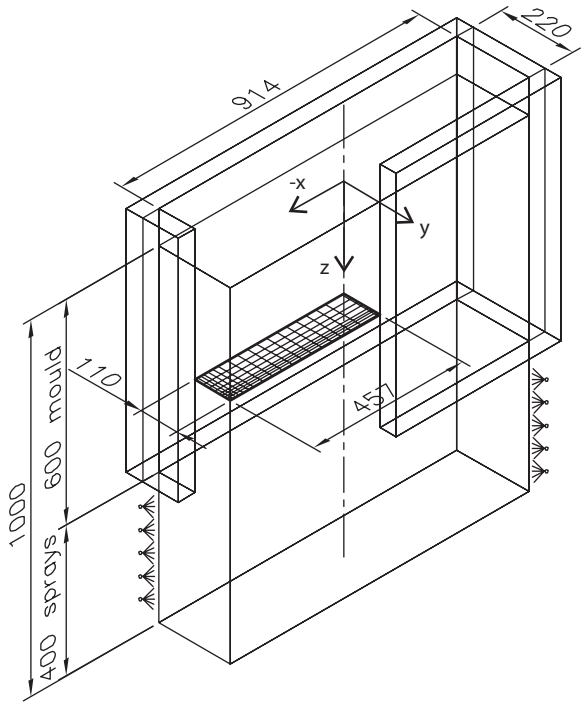

Figure 11. Slab continuous casting process. Schematic diagram (lengths are expressed in mm).

Table II. Material and problem data of the slab continuous casting simulation.

Parameter	Symbol	Value
Density	ρ	7200 kg/m^3
Specific heat	C_p	680 J/(kg °C)
Latent heat	L	272 000 J/kg
Conductivity (solid)	κ_s	34 W/(m °C)
Conductivity (liquid)	κ_l	68 W/(m °C)
Solidus temp.	θ_s	1518°C
Liquidus temp.	θ_l	1532°C
Zero Strength temp.	ZST	1518°C
Pouring temp.	θ_p	1562°C

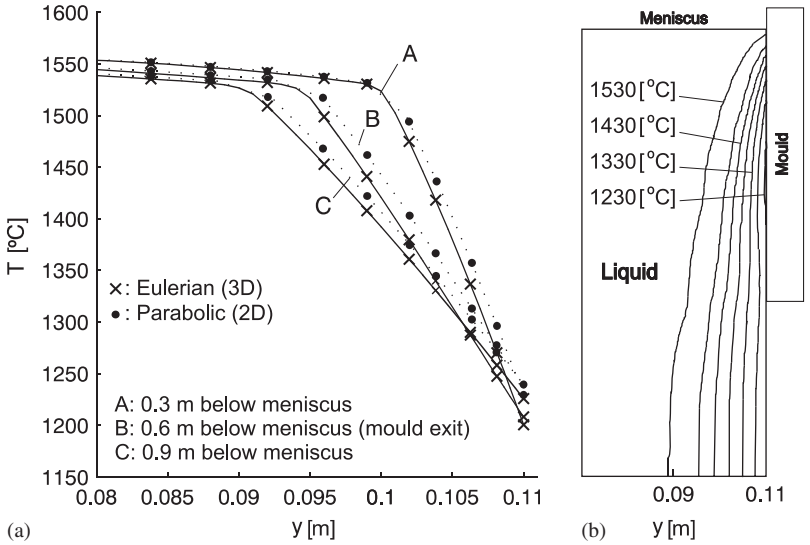

Figure 12. Slab continuous casting problem. Temperatures in the slab wide face mid-section: (a) temperatures along axis y at different times; and (b) temperature profiles.

The casting speed is 1.0 m/s and the thermal boundary conditions are:

(a) Prescribed flow in the mould–slab interface (using Savage–Pritchard law [40, 43], Δz(m))

$$q(\mathrm{MW/m^2}) = -(2.68 - 2.58\sqrt{\Delta z}) \tag{28}$$

By following Thomas *et al.* [43], we decreased this flow value by a factor 0.67 in a vertical band of 31 mm wide starting from the slab corner, because in this zone the air gap grows causing a diminution of the slab-to-mould heat conduction.

(b) Convective flux due to sprays [42] (using $h_s = 0.5\,\mathrm{MW/(m^2\,°C)}$ and $\theta_{\mathrm{spray}} = 40°\mathrm{C}$):

$$q = h_s(\theta_{\mathrm{surface}} - \theta_{\mathrm{spray}}) \tag{29}$$

An elastoplastic material model, with temperature-dependent parameters as shown in Figure 7(b), is used for the mechanical simulation. The solution was computed using the two-dimensional QUAD4_EPSC finite element of Section 2.1.

Figure 12 displays plots of the computed temperature distribution in the slab. Again, we compare solutions obtained using a parabolized 2D procedure, in which heat conduction in the z direction is neglected, and using a fixed domain method with an Eulerian (hyperbolic) 3D description [25]. We can see good agreement between both solutions.

As seen in Figure 13(a), the evolution of the stress component σ_x in the upper zone of the mould is different from that predicted by Weiner's model. This can be explained considering that in the present model we use a more realistic thermal boundary condition based on Savage–Pritchard law, while Weiner and Boley used a constant surface temperature. The difference is less important in zones near and below the mould exit, where surface temperatures are more uniform.

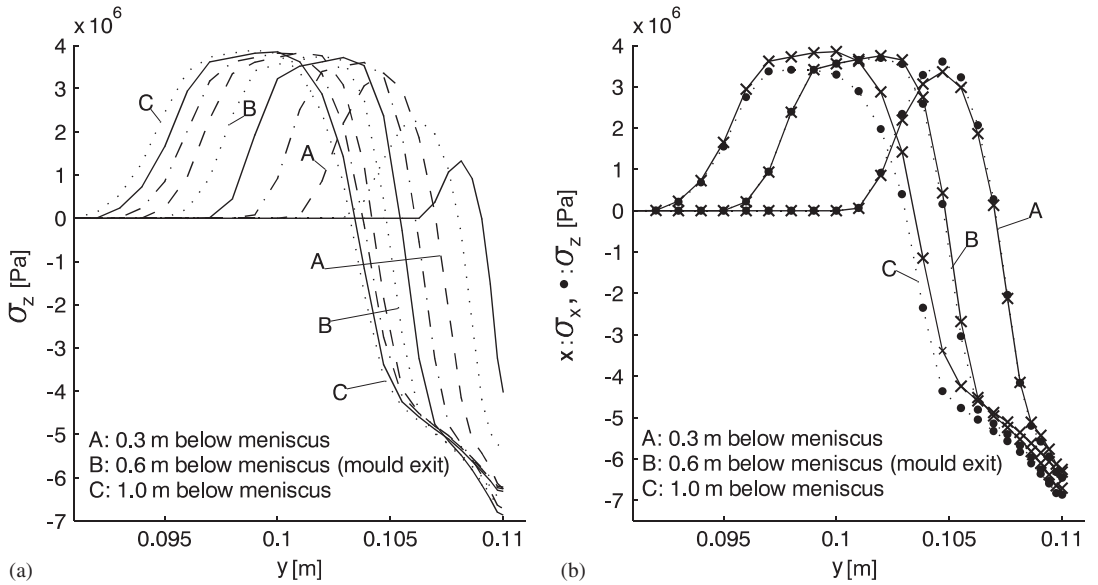

Figure 13. Slab continuous casting problem: (a) evolution of σ_x stress component in the wide face mid-section (every 0.1 m); and (b) comparison of σ_x and σ_z stress components in the wide face mid-section.

Calculated values of σ_x and σ_z in the wide face mid-section are very similar, as seen in Figure 13(b).

Figure 14 shows a detail of the distribution of axial stresses σ_z in three different sections of the corner slab along the strand. A careful analysis of them is mandatory because the largest values of stress appear in this zone. Furthermore, we note that tensile stresses appear on the shell surface at the corner of the slab, while in the remaining parts of the slab surface compressive stresses develop.

The analysis of equivalent plastic strains in Figures 15 and 16 shows values which are two times larger in the corner zones than in the face mid-section. Moreover, we see equivalent plastic strain peaks appearing in two bands, parallel to the corner's edge. Industrial experience tells us that this zone is prone to imperfections.

6. COMPARISON OF COMPUTATIONAL COST

In order to compare the computational costs of 2D EPSC and 3D formulations, similar analyses were conducted in a 1.6 MHz Pentium IV computer with 1 Gb of RAM memory, using Linux operating system. The comparison was made using a small model in order to avoid memory pagination in the 3D model: 30 time-steps with a mesh of 740 nodes for the 2D analysis, and a structured mesh of 30 layers by 740 nodes for the 3D analysis. The elapsed time to complete the test was 4 min for the 2D analysis and 78 min for the 3D analysis. The maximum usage of memory was 50 Mb for the 2D model and 850 Mb for the 3D model.

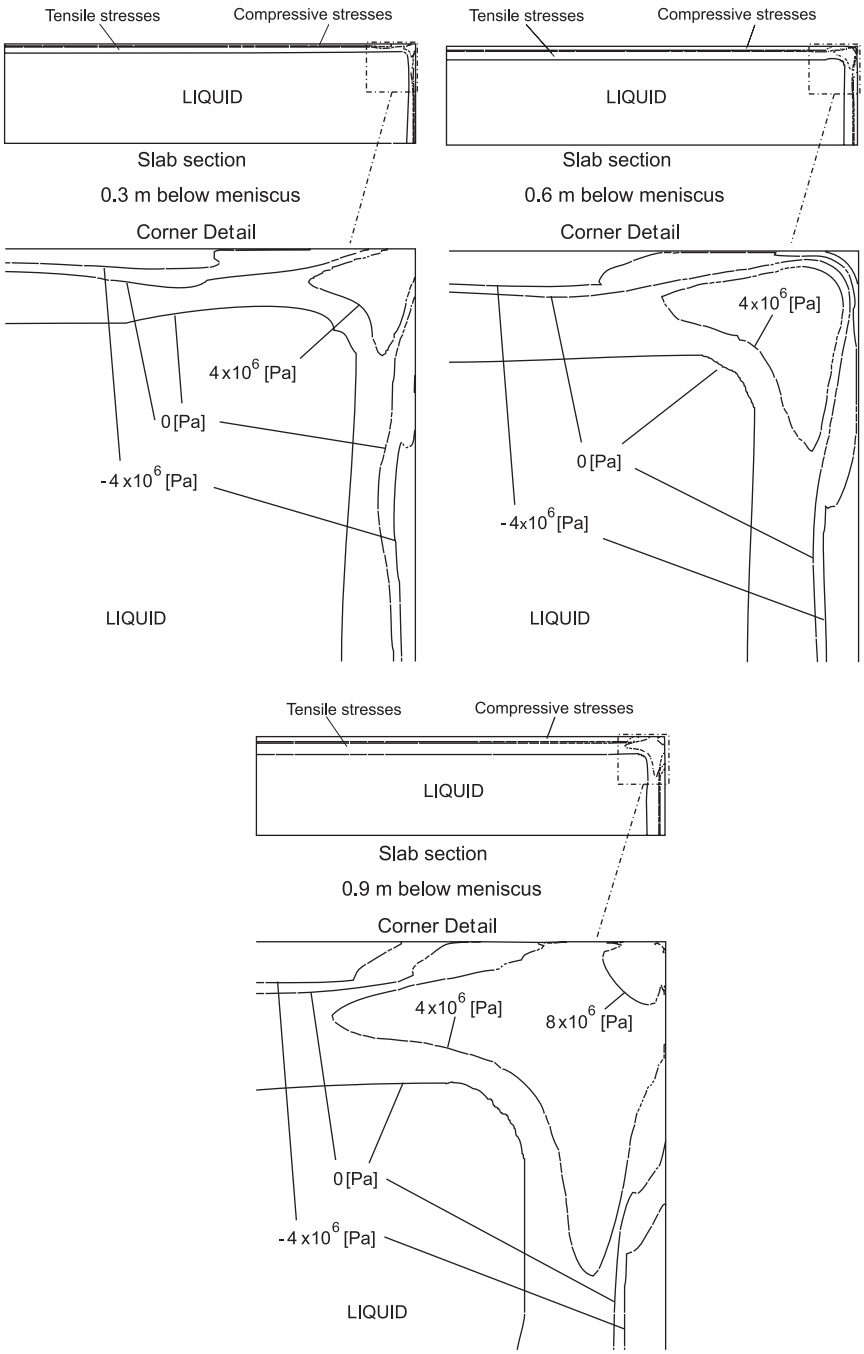

Figure 14. Slab continuous casting problem. Evolution of σ_z stresses during solidification.

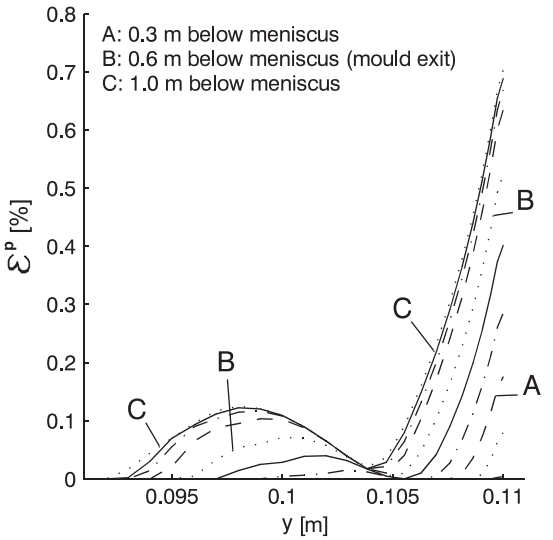

Figure 15. Slab continuous casting problem. Evolution of the wide face mid-section equivalent plastic strains.

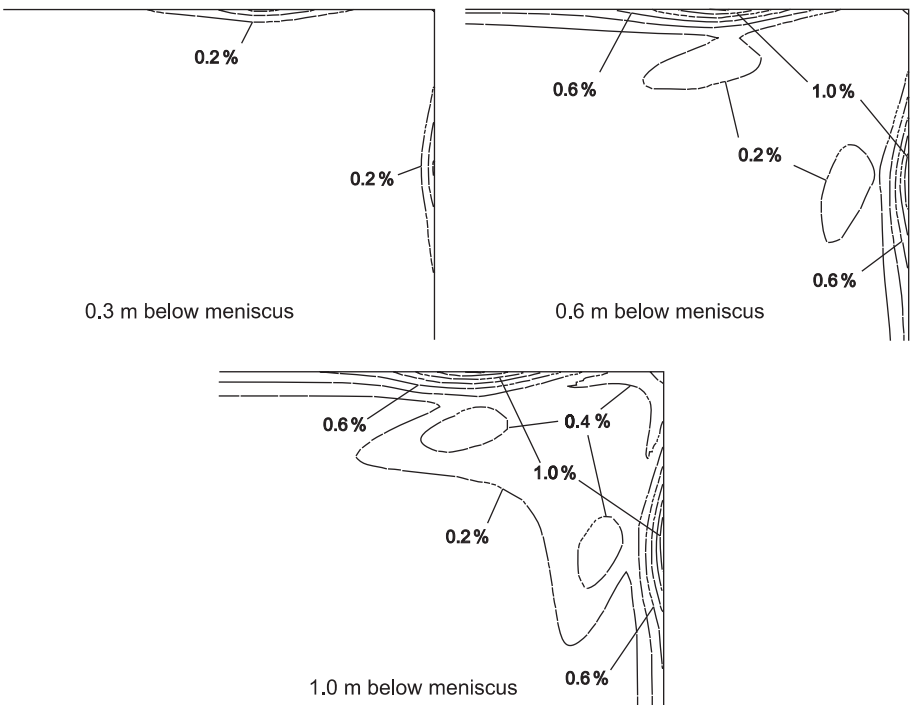

Figure 16. Slab continuous casting problem. Evolution of equivalent plastic strains close to the slab corner.

Such difference is very important in terms of application of these models to solve industrial problems. The 2D EPSC model allowed us to perform a complete thermomechanical simulation of 1 m of slab casting (including mould and primary sprays zone), by solving 100 steps with a mesh of 2622 nodes in 63 min and using only 179 Mb of memory on the same computer. Industrial cases of square billet casting, simulating the first 10 m of the strand (metallurgical length), were solved in 12 h doing 750 steps with a mesh of 2600 nodes.

7. CONCLUDING REMARKS

Two models for thermomechanical analysis of continuous casting processes have been presented and discussed. Comparisons of results were made for different industrial cases of steel continuous casting.

The following conclusions are drawn from the study:

(a) The semi-analytical solution of Weiner and Boley describes a correct trend in the distribution of stresses, in the centre of casting of round billets and at the centre of the wide side in the casting of slabs. However, the peak stresses in different sections along the strand, a fundamental result for crack analysis, are predicted incorrectly by this semi-analytical analysis essentially due to the oversimplified boundary conditions of the thermal problem.

(b) The numerical solution obtained with the EPSC model imposing a Savage–Pritchard law in the thermal problem boundary, and using realistic temperature-dependent mechanical parameters, represents well the round billet continuous casting results obtained with the Eulerian–Lagrangian model. The thermal results match well, and there is no observable difference when the time–space discretizations are similar. The mechanical results show good agreement, except in the mould exit region where stress state is fully 3D. The fields of equivalent plastic strain compare well, and the difference in stresses does not invalidate its application for its use in a subsequent crack analysis determination.

The degree of agreement between the mechanical EPSC model results and the Eulerian–Lagrangian one in the simulation of round billet continuous casting, gives us a good basis to justify its application to the simulation of slab continuous casting processes.

A remarkable characteristic of the EPSC model is its low computational cost. This makes the EPSC model suitable for future research work involving determination of parameters for cracking susceptibility.

ACKNOWLEDGEMENTS

Financial support from Agencia Nacional de Promoción Científica y Tecnológica, Argentina, through grant PID 99-76, from Consejo Nacional de Investigaciones Científicas y Técnicas, through grant PIP 0266/99, and from Universidad Nacional del Litoral, through grant CAI+D PE 214, is gratefully acknowledged.

REFERENCES

1. Yamanaka A, Nakajima K, Okamura K. Critical strain for internal crack formation in continuous casting. *Ironmaking and Steelmaking* 1995; **22**(6):508–512.

2. Kim K, Yeo T, Oh KH, Lee DN. Effect of carbon and sulfur in continuously cast strand on longitudinal surface cracks. *ISIJ International* 1996; **36**(3):284–289.
3. Won YM, Kim KH, Yeo T, Oh KH. Effect of cooling rate on ZST, LIT and ZDT of carbon steels near melting point. *ISIJ International* 1998; **38**(10):1093–1099.
4. Won YM, Han HN, Yeo T, Oh KH. Analysis of solidification cracking using the specific crack susceptibility. *ISIJ International* 2000; **40**(2):129–136.
5. Bernard C, Hiebler H, Wolf M. Simulation of shell strength properties by the SSCT test. *ISIJ International* 1996; **36**(Suppl.):S163–S166.
6. Clyne TW, Wolf M, Kurz W. The effect of melt composition on solidification cracking of steel, with particular reference to continuous casting. *Metallurgical and Materials Transactions B* 1982; **13B**:259–266.
7. Nakagawa T, Umeda T, Murata J, Kamimura Y, Niwa N. Deformation behaviour during solidification of steels. *ISIJ International* 1995; **35**(6):723–729.
8. Weiner JH, Boley BA. Elasto-plastic thermal stresses in a solidifying body. *Journal of the Mechanics and Physics of Solids* 1963; **11**:145–154.
9. Kristiansson JO. Thermal stresses in the early stage of solidification of steel. *Journal of Thermal Stresses* 1982; **5**:315–330.
10. Yu CH, Suzuki M, Shibata H, Emi T. Simulation of crack formation on solidifying steel shell in continuous casting mould. *ISIJ International* 1996; **36**:S159–S162.
11. Boehmer J, Funk G, Jordan M, Fett F. Strategies for coupled analysis of thermal strain history during continuous casting solidification process. *Advances in Engineering Software* 1998; **29**:679–697.
12. Han HN, Lee JE, Yeo T, Won YM, Kim K, Oh KH, Yoon JK. A finite element model for 2-dimensional slice of cast strand. *ISIJ International* 1999; **39**(5):445–454.
13. Bellet M, Heinrich A. A two-dimensional finite element thermomechanical approach to a global stress–strain analysis of steel continuous casting. *ISIJ International* 2004; **44**(10):1686–1695.
14. Bourdouxhe M, Charlier R, Cescotto S. A finite element for thermo-mechanical problems. In *Second International Conference on Numerical Methods in Industrial Forming Processes*, vol. 1, Mattiason K, Samuelsson A, Wood RD, Zienkiewicz OC (eds). Balkema: Rotterdam, 1986; 97–102.
15. Moitra A, Thomas B, Zhu H. Application of a thermo-mechanical finite element model of steel shell behaviour in the continuous slab casting mold. *Proceedings of the 76th Steelmaking Conference*, *ISS*, vol. 76, 1993; 657–667.
16. Thomas BG. Issues in thermal-mechanical modeling of casting processes. *ISIJ International* 1995; **35**(6): 737–743.
17. Thomas BG, Parkman JT. Simulation of thermal mechanical behaviour during initial solidification. *Thermec '97 International Conference on Thermomechanical Processing of Steel and Other Materials*, Wollongong, Australia, 1997; 7–11.
18. Pascon F. 2d1/2 thermal-mechanical model of continuous casting of steel using the finite element method. *Ph.D. Thesis*, University of Liège, Belgium, 2003.
19. Li C, Thomas BG. Thermo-mechanical finite element model of shell behaviour in continuous casting of steel. *Metallurgical and Materials Transactions B* 2004; **35**(6):1151–1172.
20. Heaton MD. A calculation of the elastic constants of a unidirectional composite containing transversely isotropic fibres. *Journal of Physics D*: *Applied Physics* 1970; **3**:672–676.
21. Vel SS, Batra RC. A generalized plane strain deformation of thick anisotropic composite laminate plates. *International Journal of Solids and Structures* 2000; **37**(5):715–733.
22. Fachinotti VD. Modelado numérico de fenómenos termomecánicos en la solidificación y enfriamiento de aceros obtenidos por colada continua. *Doctoral Tesis*, Universidad Nac. Litoral, Argentina, 2001.
23. Fachinotti VD, Cardona A. A fixed-mesh Eulerian–Lagrangian approach for stress analysis in continuous casting. *International Report*, CIMEC, sent to *IJNME*, 2002.
24. Fachinotti VD, Cardona A, Huespe AE. A fast convergent and accurate temperature model for phase-change heat conduction. *International Journal for Numerical Methods in Engineering* 1999; **44**(2):1863–1884.
25. Fachinotti VD, Cardona A, Huespe AE. Numerical simulation of conduction–advection problems with phase-change. *Latin American Applied Research* 2001; **31**:31–36.
26. Lewis RW, Brass BR. The determination of stresses and temperatures in cooling bodies by finite elements. *Journal of Heat Transfer* 1976; **98**(3):478–485.
27. Lewis RW, Morgan K, Roberts PM. Determination of thermal stresses in solidification problems. In *Numerical Analysis of Forming Processes*, Pittman JFT, Zienkiewicz OC, Wood RD, Alexander JM (eds). Wiley: New York, 1984; 405–431 (Chapter 15).

28. Huespe AE, Cardona A, Fachinotti VD. Thermomechanical model of a continuous casting process. *Computer Methods in Applied Mechanics and Engineering* 2000; **182**:439–455.
29. Williams JR, Lewis RW, Morgan K. An elasto-viscoplastic thermal stress model with applications to the continuous casting of metals. *International Journal for Numerical Methods in Engineering* 1979; **14**(1):1–9.
30. Kozlowski PF, Thomas BG, Azzi JA, Wang H. Simple constitutive equations for steel at high temperature. *Metallurgical and Materials Transactions A* 1992; **23**:903–918.
31. Fachinotti VD, Cardona A. Constitutive models of steel under continuous casting conditions. *Journal of Materials Processing Technology* 2003; **135**:30–43.
32. Simo JC, Hughes TJR. *Computational Inelasticity*. Springer: Berlin, 1998.
33. Nakato H, Sakuraya T, Nozaki T, Emi T, Nishikawa H. Physical and chemical properties of casting powders affecting the mold lubrication during continuous casting. In *Mold Powders for Continuous Casting and Bottom Pour Teeming*, Harry G (ed.), ISS, 1987; 23–29.
34. Mazumdar S, Ray SK. Solidification control in continuous casting of steel. *Sadhana* 2001; **26**:179–198.
35. Cardona A, Klapka I, Géradin M. Design of a new finite element programming environment. *Engineering Computations* 1994; **11**:365–381.
36. Klapka I, Cardona A, Géradin M. An object-oriented implementation of the finite element method for coupled problems. *Revue Européenne des Éléments Finis* 1998; **7**(5):469–504.
37. Li C, Thomas B. Thermo-mechanical finite element model of shell behaviour in the continuous casting of steel. *Proceedings of the 6th Asia-Pacific Symposium on Engineering Plasticity and its Applications* 2002; **1**:827–834.
38. Kelly JE, Michalek KP, O'Connor TG, Thomas BG, Dantzig JA. Initial development of thermal and stress fields in continuously cast steel billets. *Metallurgical and Materials Transactions A* 1982; **19A**:2589–2602.
39. Perez T, Goldschmit M, Dvorkin E, Nigro N, Storti M, Idelsohn S. Segregación dendrítica de aceros obtenidos por colada contínua. iii. Resolución numérica de la macrosegregación en un acero 1040 fabricado por Siderca. *Reporte Técnico CINI-FUDETEC GTM-INTEC Septembre 1997*, 1997.
40. Linacre ET, Crane JC. Heat transfer rate in a water-cooled mould. In *The Problem of the Rupture of the Billet in the Continuous Casting of Steel*, Savage J, Pritchard WH (eds). *Journal of the Iron and Steel Institute* 1952; **178**:269–277.
41. Dvorkin E, Canga M. Thermomechanical behaviour of the mold in Siderca continuous casting machine CC3. Case of ϕ295 mm and carbon steel 042. *Reporte Técnico I 1.20/190-90*, CINI, 1990.
42. El-Bealy M. On the mechanism of halfway cracks and macro segregation in continuously cast steel slabs. I. Halfway cracks. *Scandinavian Journal of Metallurgy* 1995; **24**:63–80.
43. Thomas BG, Li G, Moitra A, Habing D. Analysis of thermal and mechanical behaviour of copper molds during continuous casting of steel slabs. *ISS Transactions* 1998; 125–143.

